Azadeh Jafari, Farzin Ghanadi, Maziar Arjomandi, Matthew J. Emes, Benjamin S. Cazzolato

Correlating turbulence intensity and length scale with the unsteady lift force on flat plates in an atmospheric boundary layer flow

Journal of Wind Engineering and Industrial Aerodynamics, 2019; 189:218-230

Final publication at http://dx.doi.org/10.1016/j.jweia.2019.03.029

Correlating turbulence intensity and length scale with the unsteady lift force on flat plates in an atmospheric boundary layer flow

Azadeh Jafari*, Farzin Ghanadi, Maziar Arjomandi, Matthew J. Emes, Benjamin S. Cazzolato

School of Mechanical Engineering, University of Adelaide, Adelaide, Australia

Abstract

The correlation between turbulence intensity and length scale and the lift force on a horizontal flat plate in an atmospheric boundary layer flow is investigated in this study. Experiments were conducted in a large-scale wind tunnel to measure the peak loads on flat plate models of various chord length dimensions at different heights within simulated atmospheric boundary layers. The peak lift force coefficient on the flat plates was correlated with both turbulence intensity and length scale. The results show that the peak lift force coefficient on the flat plate is a function of vertical integral length scale (L_w^x) and vertical turbulence intensity (I_w) in terms of a parameter defined as $I_w(\frac{L_w^x}{c})^{2.4}$, where c is the chord length of the plate. An increase in this turbulence parameter from 0.005 to 0.054, increases the peak lift force coefficient from 0.146 to 0.787. The established relationship is then used to predict the peak wind loads on full-scale heliostats within the atmospheric surface layer as a case study. It is found that decreasing the ratio of heliostat height to the chord length dimension of the mirror panel from 0.5 to 0.2 leads to a reduction of 80% in the peak stow lift force coefficient, independent of the terrain roughness.

Keywords: Wind load, turbulence intensity, integral length scale, atmospheric boundary layer, Heliostat.

Nomenclature

A	Plate area (m^2)
c	Plate chord length dimension (m)
$C_{L,p}$	Peak lift force coefficient
$C_{L,p(0.5)}$	Peak lift force coefficient for H/c=0.5
F_L	Lift force (N)
f	Frequency (Hz)
H	Height (m)
I_u	Longitudinal turbulence intensity (%)
I_w	Vertical turbulence intensity (%)
L_u^x	Longitudinal integral length scale (m)
L_w^x	Vertical integral length scale (m)

p	Pressure (Pa)
R	Autocorrelation of velocity
S_u	Power spectral density of the longitudinal velocity fluctuation (m^2/s)
t	Time (s)
τ_u^x	Longitudinal integral time scale of turbulence (s)
U_∞	Free-stream velocity (m/s)
u, v, w	Absolute velocity components in the $x-, y-, z-$ flow directions, respectively (m/s)
U, V, W	Time averaged mean velocity components in the $x-, y-, z-$ flow directions, respectively (m/s)
u', v', w'	Fluctuating velocity components in the $x-, y-, z-$ flow directions, respectively (m/s)
x, y, z	Distance in the stream-wise, lateral and vertical directions (m)
z_0	Aerodynamic surface roughness length (m)
Symbols	
σ_u	Standard deviation of longitudinal velocity fluctuations (m/s)
η	Turbulence parameter
ρ	Density (kg/m^3)
φ	Angle of attack (rad)

1 Introduction

The turbulence within the atmospheric boundary layer (ABL) induces highly fluctuating aerodynamic loads on the structures within the ABL. An accurate estimation of the wind loads on structures is of high significance for their design. Wind loads on large civil structures such as buildings and bridges have been studied thoroughly in the literature. However, their design guidelines are not applicable to small-scale structures such as solar panels and heliostats. While these structures, which are placed at lower 10–20 m within the atmospheric surface layer (ASL), are exposed to highly turbulent wind conditions, the effect of atmospheric turbulence on their wind loads is not well known. With the increasing popularity of solar energy and the growth of solar panels and concentrating solar power plants, it is important to provide an accurate prediction of the wind loads on them since underestimation of the peak loads in the design process will lead to overstressing and consequently structural failure (Peterka, Tan, *et al.*, 1987). A common practice for reducing wind loads during extreme wind gusts is stowing the heliostats and solar trackers by aligning the mirror panel horizontally. In a turbulent flow such as the ASL, the significant force on stowed heliostats and solar trackers is the lift force which is caused by the variations in the pressure distribution on the upper and lower faces of the mirror panel as a turbulent eddy passes over it, as shown schematically in Figure 1. The lift force then induces a bending moment at the base of the pylon which is important for the design of solar trackers and heliostats. This study aims to investigate the effect of turbulence on the peak lift force on stowed heliostats and solar trackers, which can be represented by horizontal flat plates with a large ratio of characteristic length to thickness.

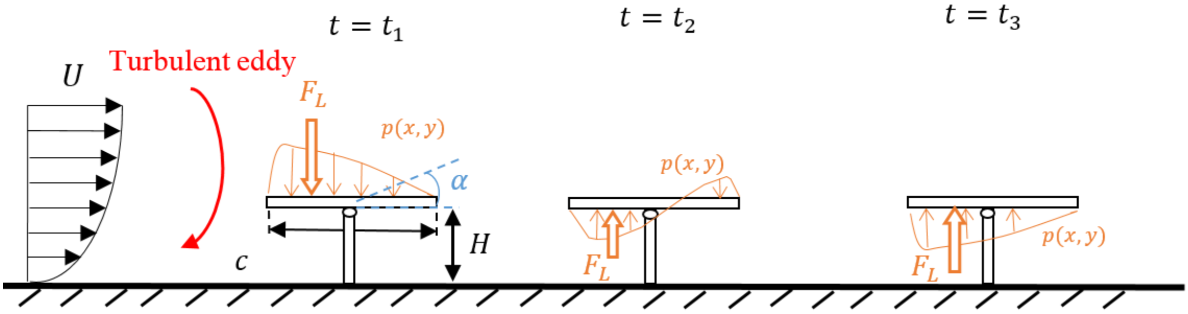

Figure 1: Fluctuating pressure distribution on a stowed heliostat within the atmospheric boundary layer based on the pressure measurements from (Emes *et al.*, 2017; Gong *et al.*, 2013) (Instantaneous pressure distributions at three random time steps are shown).

Wind loads on flat plates in boundary layer flows are found to increase dramatically with increasing turbulence intensity as indicated by wind tunnel experiments presented in the literature (Emes *et al.*, 2017; Emes *et al.*, 2018; Peterka *et al.*, 1989; Pfahl *et al.*, 2011). Peterka, Tan, *et al.* (1987) measured the wind loads on heliostat models within a simulated boundary layer in a wind tunnel, and found that the peak lift force coefficient on a stowed heliostat almost doubles when longitudinal turbulence intensity increases from 14% to 18%. Furthermore, it has been reported that the peak lift force coefficient on a stowed heliostat increases by 28% and 77% when the longitudinal turbulence intensity increases from 13% to 21% (Pfahl *et al.*, 2015) and from 7% to 26% (Jafari *et al.*, 2017), respectively. Emes *et al.* (2017) found that the peak lift force coefficient increases linearly as the longitudinal turbulence intensity increases from 10% to 14%. The reason for this dramatic effect is not yet known. Furthermore, there are discrepancies between the peak lift force coefficients on stowed heliostats reported by the different studies which were measured at similar turbulence intensities. As the peak lift force coefficient on a stowed heliostat at I_u=18% is reported to be 0.9 by Peterka, Tan, *et al.* (1987), in contrast to 0.49 by Pfahl *et al.* (2015). Also, according to Pfahl *et al.* (2015), the peak lift coefficient equals 0.46 at I_u=13%, while Emes *et al.* (2017) reports a coefficient of 0.83 at I_u=12.5%. On the other hand, Pfahl (2018) proposed that that the peak and fluctuating lift force coefficients on a stowed heliostat depend on the vertical turbulence intensity, not the longitudinal one. This argument is, however, not well-established as both longitudinal and vertical turbulence intensities varied in the experiments by Pfahl (2018). Since in all the mentioned studies, both longitudinal and vertical turbulence intensities changed simultaneously, it not clear whether the observed effects were due to longitudinal turbulence intensity or vertical turbulence intensity. Therefore, this study aims to provide a deeper understanding of the effect of turbulence intensity on the peak lift force coefficient on a horizontal flat plate in terms of determination of the dominant turbulence component, i.e. longitudinal or vertical.

Another parameter which is found to affect the wind loads is the integral length scale of turbulence which expresses the average size of the most energetic eddies within the turbulent flow and is a key factor influencing the loads on bluff bodies within a turbulent flow (Bearman and Morel, 1983). The drag coefficient on a flat plate normal to a turbulent flow is found to be strongly dependent on the relative size of the longitudinal integral length scale to the chord length dimension of the plate (Bearman, 1971). The root-mean-square (RMS) of the drag coefficient increases dramatically by decreasing the plate's chord length, which as taken equal to increasing L_u^x/c (Bearman, 1971). Measurement of the spectra of the unsteady longitudinal velocity component upstream of the stagnation point and its comparison with the spectra in the absence of the plate shows distortion of turbulence along the stagnation line, such that the small scale turbulence is amplified and the large scales are attenuated (Bearman and Morel, 1983). The distortion of turbulence when approaching a bluff body is postulated to depend on L_u^x/c. According to Holdø et al. (1982), when the integral length scale is much larger than the chord length of the plate, the flow behaviour is quasi-static and the effect of the bluff body on the turbulence is similar to its effect on the mean flow. Therefore, the energy of the fluctuating longitudinal velocity component is transferred to the vertical and lateral components as the flow approaches the plate. Holdø et al. (1982) proposes that when the integral length scale is much smaller than the chord length, stretching of the vortex lines is the dominant mechanism.Hence, the fluctuating longitudinal velocity component and thereby the longitudinal turbulence intensity increase and turbulence is amplified along the stagnation line, while the vertical and lateral components remain almost constant (Holdø et al., 1982). If the integral length scale is in the same order of the body's cross-flow dimension, a combination of both effects occurs (Bearman, 1971; Holdø *et al.*, 1982). The behaviour of a flow over a thin flat plate is however different from bluff bodies. Emes *et al.* (2017) reported that the peak lift force coefficient on a stowed heliostat increases by increasing the relative size of the longitudinal integral length scale of turbulence, L_u^x, to the chord length of the heliostat panel

(L_u^x/c). However, in their experiments, both longitudinal and vertical integral length scales varied, and therefore it is not clear whether the observed increase in the peak lift force coefficient is due to the effect of L_u^x or L_w^x. The vertical length scale, L_w^x, seems to be important for a thin horizontal flat plate since the fluctuating lift is mainly dependent on the vertical velocity component (Rasmussen *et al.*, 2010). In order to provide a better understanding of the effect of longitudinal and vertical integral length scales on the lift force, it is necessary to distinguish their effects by further experimentation. Therefore, one of the aims of this study is to develop an understanding of the major contributor to the lift force, L_u^x or L_w^x, and to determine the correlation between the peak load on a horizontal flat plate in a with the integral length scale of turbulence.

Turbulence intensity and integral length scale vary with the height from the ground within the ASL. As the height in the ASL increases, the longitudinal integral length scale tends to get larger while turbulence intensity decreases (ESDU85020, 2010). Moreover, the effects of turbulence intensity and integral length scale are interrelated and cannot be separated. For instance, the peak and fluctuating pressures on a horizontal blunt flat plate (α=0°) are found to be strongly dependent on both turbulence intensity and length scale ratio such that the effect of L_u^x/c on the peak pressure is greater at higher turbulence intensities (Li and Melbourne, 1999; Shu and Li, 2017). The peak pressure on the plate which occurs near separation is found to increase with the parameter $I_u(L_u^x/c)^{0.15}$ (Li and Melbourne, 1995) where I_u and L_u^x are the turbulence intensity and integral length scale, respectively. Furthermore, the pressure coefficient on a normal flat plate (α=90°) is also a function of both turbulence intensity and L_u^x/c and increases logarithmically with the turbulence parameter $I_u(L_u^x/c)^2$ (Bearman, 1971). Hence, in order to provide an accurate prediction of wind loads on flat-plate-like structures, it is necessary to establish a correlation between the aerodynamic lift force coefficient on flat plates and both turbulence intensity and integral length scale.

The studies in the literature suggest the increase in the unsteady lift force on a horizontal flat plate with increasing turbulence intensity and integral length scales. However, none of the studies developed a strong argument, and no conclusion about the effect of turbulence was reached. While Emes *et al.* (2017); Peterka *et al.* (1989); Pfahl *et al.* (2011) proposed the longitudinal turbulence intensity to be important, Pfahl (2018) proposed the increase of the lift force to be due to the effect of vertical turbulence intensity. The main problem in the literature is that their results are simultaneously affected by both turbulence intensity and integral length scale, and both longitudinal and vertical components. For example, Emes et al. (2017) reported that increasing L_u^x/c led to increasing the peak lift coefficient. This result was obtained by measuring the forces on flat plates of different chord length dimensions at a constant flow condition, i.e. changing c to change L_u^x/c. However, it was not noted that L_w^x/c was also increasing, and the observed increase in the lift coefficient could be due to the increase of L_w^x/c. A similar limitation applies to the reported effect of I_u by Emes et al. (2017), as I_w and the integral length scales did not remain constant. As another example, Pfahl (2018) proposed that the peak lift coefficient on a stowed heliostat increased with increasing the vertical turbulence intensity, but could not differentiate the observed effect from the possible effect of longitudinal turbulence intensity as I_u increased as well. Furthermore, the integral length scales were not constant in the reported results by Pfahl (2018). Therefore, it is not yet known which turbulence component is of main impact on the fluctuating lift force on a horizontal flat plate. Hence, the objective of the present study is to develop a better understanding of the effect of turbulence intensity and length scale on the peak lift force on horizontal flat plate-like structures in the ASL. It aims to establish a correlation between the lift force with both turbulence intensity and integral length scale. To do so, the lift force on flat plates of different dimensions were measured at different heights within two simulated boundary layers in wind tunnel experiments. The turbulence characteristics of the wind tunnel boundary layers are described in Section 2. In Section 3, the experimental results are presented and a correlation between the turbulence characteristics and the wind loads is developed. The developed correlation is then used in Section 4 to predict the lift force on stowed heliostats within the ASL as a case study. Furthermore, the possibility of reduction of the lift force on a stowed heliostat by decreasing the stow height is discussed. The results of this study will contribute to a better understanding of wind loads on structures such as heliostats, solar trackers, and solar panels, and can be used to reduce wind loads on them.

2 Experimental method

Experiments were conducted in a large-scale wind tunnel at the University of Adelaide. The rectangular test section of the boundary layer wind tunnel has a cross-sectional area of 3 m × 3 m. The wind tunnel is designed for a maximum air speed of 33 m/s, and a boundary layer thickness of 0.2 m in the smooth flow at the heliostat location. The level of turbulence intensity in the empty tunnel is between 1% and 3% outside the boundary layer. As an initial stage, ABL was simulated in the wind tunnel by use of spires and roughness elements. Two sets of spires were first designed as non-truncated based on the desired power law exponent and boundary layer height using the empirical formula given by Irwin (1981). The design was then modified for part-depth simulation of the ABL based on Kozmar's part-depth method (Kozmar, 2011). In each set, three spires with identical dimensions, shown in Figure 2, were used placed at a centre-line distance of 0.9 m in the lateral direction. The flat plate model was placed downstream at a distance equal to 6 times the spire height which is expected to be sufficient for flow development (Irwin, 1981). The spires were followed by a 10 m fetch of wooden roughness elements of 90 mm × 90 mm cross section and 45 mm height. The sizing and spacing of the roughness elements were determined using the empirical equations by (Wooding *et al.*, 1973). The elements were placed with a spacing of 500 mm in all directions covering approximately 24% of the floor area over the fetch length. The experimental test setup is illustrated in Figure 3.

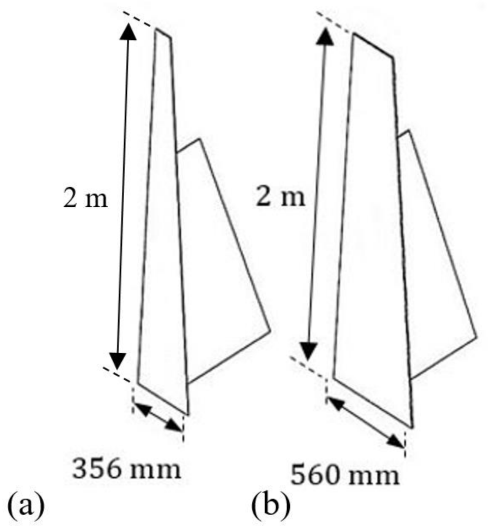

Figure 2: Dimensions of the two spire sets (a) Set 1 (b) Set 2.

The flat plate models comprise a square aluminium plate mounted on a pylon. In order to investigate the effect of height, pylons with heights of 0.14 m to 0.64 m, with an increment of 0.1 m, were built. Plates with chord lengths of 0.5 m, 0.6 m and 0.7 m and a thickness of 3 mm were used. This range of plate chord lengths and pylon heights delivered H/c ratios between 0.2 and 1.3. H/c =0.2 was the smallest ratio used in the experiments due to the technical challenges of building models with smaller H/c ratios and measuring forces on them. Heliostats and solar trackers are conventionally designed for height to chord length ratio, H/c, of about 0.5 (Téllez *et al.*, 2014). Hence, a range of H/c between 0.2 and 1.3 allowed investigation of the wind loads for higher and lower ratios.

The forces on the flat plate models were measured by three three-axis Bestech load cells (K3D50), each with a capacity of 50 N. The load cells were calibrated for a range of forces between 0-25 N. The measurement errors are found to be approximately 1.5% of the measured forces. Forces on the model were measured over a sampling period of 120 seconds, sampled at 1 kHz. It was determined through extreme value analysis that the estimated peak loads vary by less than 2% if the sampling period increases above 120 seconds. Therefore, this period was found to be sufficient. The peak values were determined based on extreme value analysis and the assumption of a Gaussian distribution as the sum of the mean value and three-times the root-mean-square of the fluctuating forces (Simiu and Scanlan, 1996). This method is used to predict the peak value from a set of data collected over a sampling time with 99.7% probability that forces will not exceed this value.

The lift force coefficient is found by the following equation:

$$C_L = \frac{F_L}{\frac{1}{2}\rho U^2 A} \tag{1}$$

where F_L represents the lift force on the plate, ρ is the air density, U is the mean velocity at plate height and $A = c^2$ represents the plate area. It must also be noted that absolute values for the lift force coefficient are given.

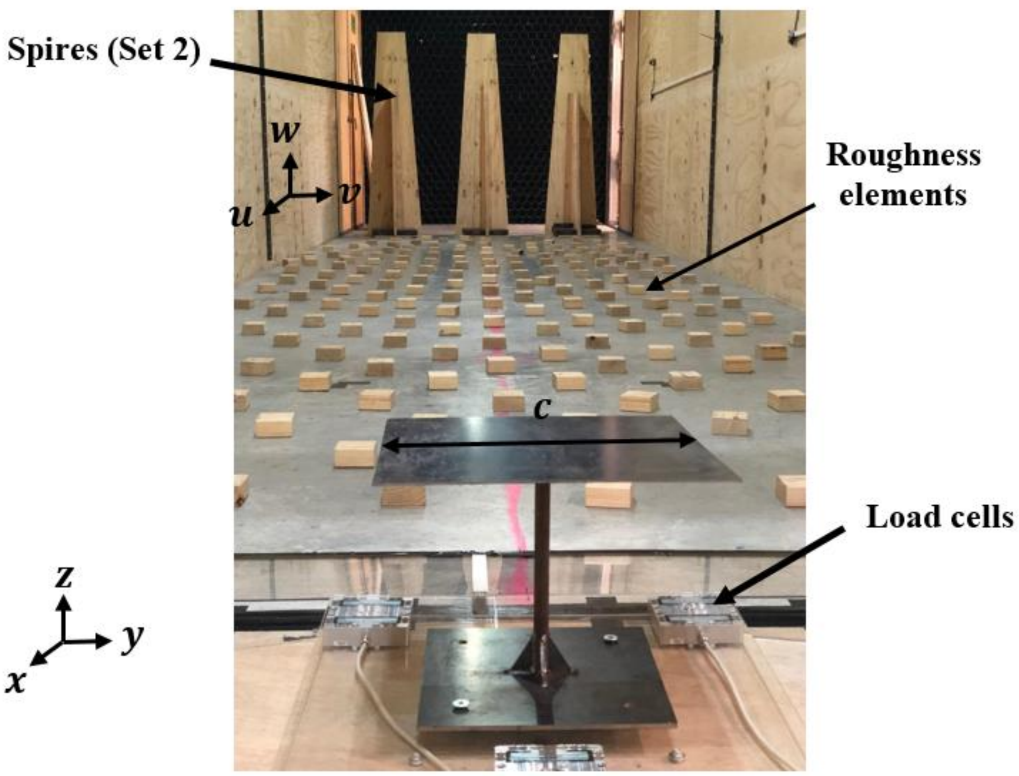

(a)

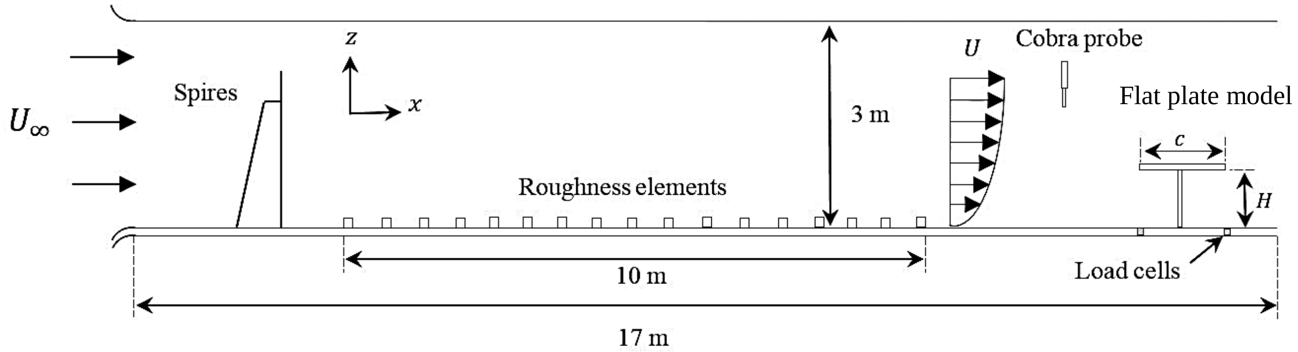

(b)

Figure 3: (a) Experimental test setup, (b) Schematic of the test section containing spires and roughness elements and the flat plate model.

2.1 Simulation of the atmospheric boundary layer

Three components of velocity (u, v, w) were measured by a Turbulent Flow Instrumentation (TFI) multihole probe (Cobra probe), with an accuracy of ±0.5 m/s. The velocity measurements were taken downstream of the roughness fetch, with a longitudinal spacing of 500 mm up to the model position, over an area of 1 m2 in both vertical and lateral directions, in order to investigate flow development. The flow characteristics at the model position and in the absence of the flat plate model are reported in this section. Data were sampled at a rate of 1 kHz for a duration of 150 s at each location. In order to reduce the experimental errors, the velocity measurements were repeated for five times and the average of five measurements was calculated. Figure 4 shows the mean velocity profile as a function of height at three lateral locations in the wind tunnel boundary layers using the two spire sets (hereafter referred to as WTBL1 and WTBL2) at a freestream velocity of 11.5 m/s. The shaded areas in Figure 4 show the heights where the flat plate models were placed within the wind tunnel (z=0.14 m to 0.64 m). The mean velocity at the centre line (y=0) shows a maximum of 9% and 14% deviation from the side lines (y=−0.5, y=0.5) at the position of the heliostat model for WTBL1 and WTBL2, respectively. The velocity profiles of WTBL1 show a better lateral homogeneity than WTBL2 which is due to the higher separation and turbulence produced by the spires of Set 2. As the flat plate models are placed at a maximum lateral distance of 0.3 m from the centre line, the lateral homogeneity of both simulated boundary layers is acceptable and the measured velocity at the centre line is used for calculation of wind loads.

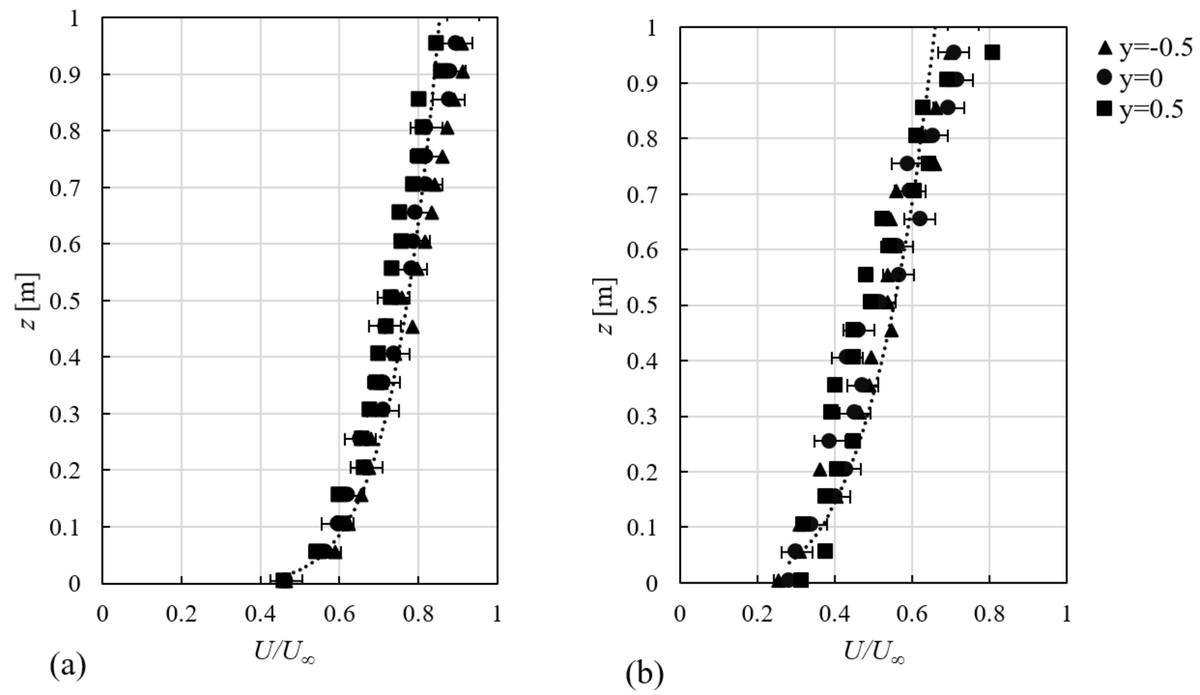

Figure 4: Mean velocity profiles normalised with respect to the reference velocity (U_∞=11.5 m/s) at three lateral locations for (a) WTBL1, Spire Set 1, (b) WTBL2, Spire Set 2, in model scale (The shaded area shows the height of the flat plate models in the wind tunnel).

Figure 5(a) shows the mean velocity profiles at the centre-line (y=0) of the wind tunnel measured at heights up to 1 m compared to the logarithmic profiles of the mean wind velocity within the ABL. The velocity profile of the boundary layer generated by Spire Set 1 matches a logarithmic profile with a roughness height of 0.018 m in full scale, with a maximum error of 2.3%. The mean velocity profile of WTBL2 represents a logarithmic profile with a roughness height of 0.35 m and a displacement height of 0.02 m in full scale, with a maximum error of 5% at the model position. Therefore, the mean velocity profiles of WTBL1 and WTBL2 provide a good representation of the mean wind velocity for z_0=0.018 m and z_0=0.35 m, respectively. The aerodynamic surface roughness lengths were determined from fitting the mean velocity profile of each simulation to the logarithmic law. It must be noted that as suggested by (De Paepe *et al.*, 2016; Holmes, 2007; Kozmar, 2012) the displacement height is negligible for flat and open country terrains whose surface roughness value is low while for suburban and urban areas with larger surface roughness, the displacement height must be taken into account. Therefore, the displacement height is only considered in the log law profile for WTBL2 with z_0=0.35 m, and it is considered negligible for WTBL1 which represents an open country terrain with z_0=0.018 m. Comparison of the mean velocity profiles with the power law profiles, as shown in Figure 5(b), also indicates that the boundary layer generated by Spire Set

1 matches a power law for α=0.18 and WTBL2 represents a power law profile for α=0.3. The power-law profiles in Figure 5(b) were determined by assuming a reference height within each boundary layer. According to De Paepe et al. (2016), an arbitrary height within the simulated boundary layer can be used as the reference for part-depth simulated boundary layers. the reference height was chosen as z_{ref} =1 m, as it is not in the vicinity of the ground or the ceiling of the tunnel, and is therefore not affected by the local effects of the roughness elements or the secondary boundary layer formed over the ceiling (De Paepe et al., 2016). Furthermore, this height is larger than the height of the flat plate models in the wind tunnel. The mean velocity obtained at different heights of each boundary layer are then normalised with the mean velocity at the reference height, which equals 10.87 m/s and 9.95 m/s for WTBL1 and WTBL2, respectively.

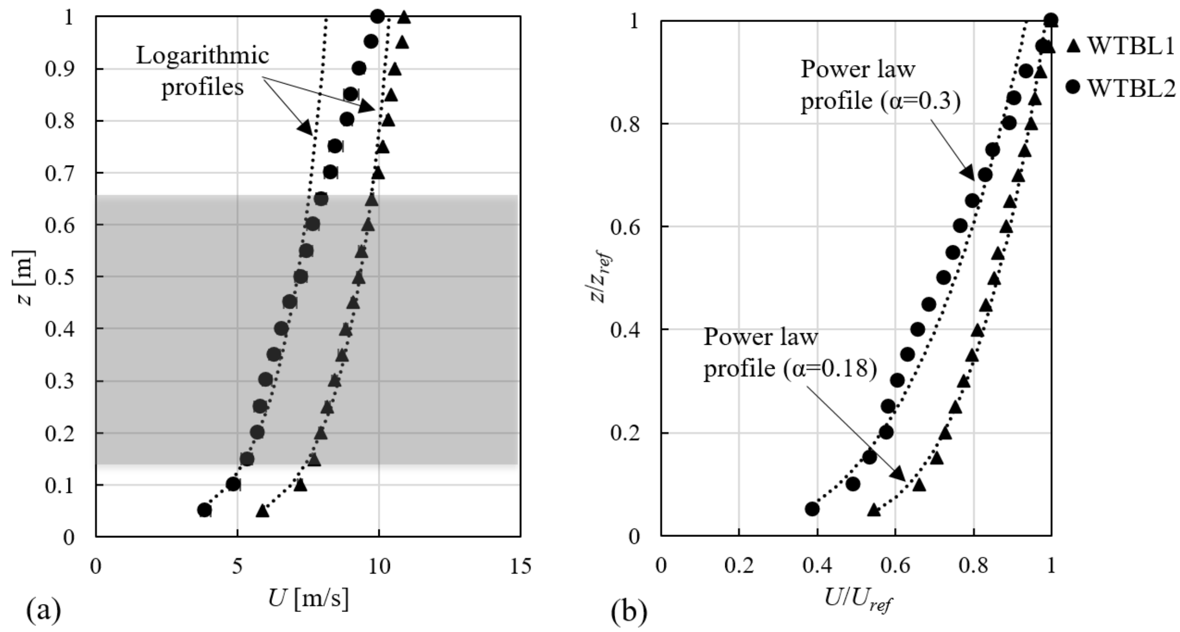

Figure 5: Mean velocity profile of the boundary layers generated by the two spire sets in the wind tunnel in model scale, (a) comparison with logarithmic profiles. The error bars show the standard deviation calculated from five measurements, (b) comparison with power law profiles (The shaded area shows the height of the flat plate models in the wind tunnel).

In order to compare the characteristics of the wind tunnel boundary layers with the ASL, the simulation length scale factor was calculated for each boundary layer. The length scale factor was calculated using Cook's method (Cook, 1978) from the aerodynamic surface roughness length and integral length scales at different heights within each boundary layer. The length scale factor of each boundary layer was then determined as the average of the calculated values for different heights. Hence, the simulation length scale factor was found to equal 1:151 and 1:90 for WTBL1 and WTBL2, respectively.

The turbulence characteristics of the flow in the two wind tunnel boundary layers including turbulence intensity, power spectral density and integral length scales are determined. The turbulence intensity is calculated based on the measured velocity for heights up to 1 m in the wind tunnel for WTBL1 and WTBL2. Figure 6 shows the longitudinal and vertical turbulence intensity profiles achieved in WTBL1 and WTBL2 in the wind tunnel scale. The longitudinal turbulence intensity at the heights where the flat plate model is positioned (*z*=0.14 m to 0.64 m) in the wind tunnel is between 11% and 13% and between 24% and 28% for the WTBL1 and WTBL2, respectively. The vertical turbulence intensity at the model height in the wind tunnel is about 9% for the WTBL1, and is about 19% for the WTBL2. Turbulence intensity profiles from the wind tunnel measurements for heights up to 1 m are converted to match the full scale height using the simulation length scale factors, 1:151 and 1:90 for WTBL1 and WTBL2, respectively. Turbulence intensity for a similar terrain type to each WTBL was estimated according to ESDU85020 (2010) and (ESDU74031, 1974). The longitudinal and vertical turbulence intensity profiles from WTBL1 and WTBL2 are shown in Figure 6(b-c) and Figure 6(d-e), respectively. The solid and dashed lines show the upper and lower bounds of the ESDU 74031 and ESDU 85020 ranges, respectively, which are represented as ±20% from the calculated mean values which is suggested as the allowable bandwidth (ESDU85020, 2010). According to Figure 6(b-d), both longitudinal and vertical turbulence intensity profiles of WTBL1, and the longitudinal turbulence intensity in WTBL2 are within the ESDU range. The vertical turbulence intensity for WTBL2 is, however, larger than the ESDU estimations (Figure 6(e)).

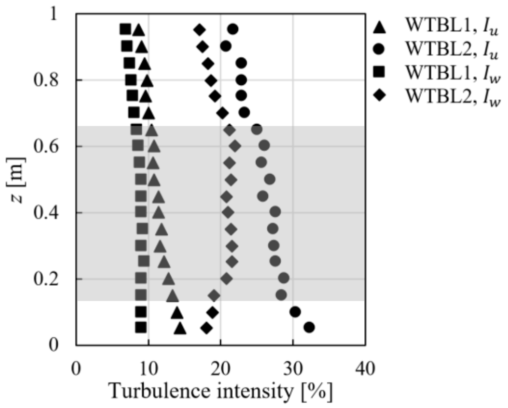

(a)

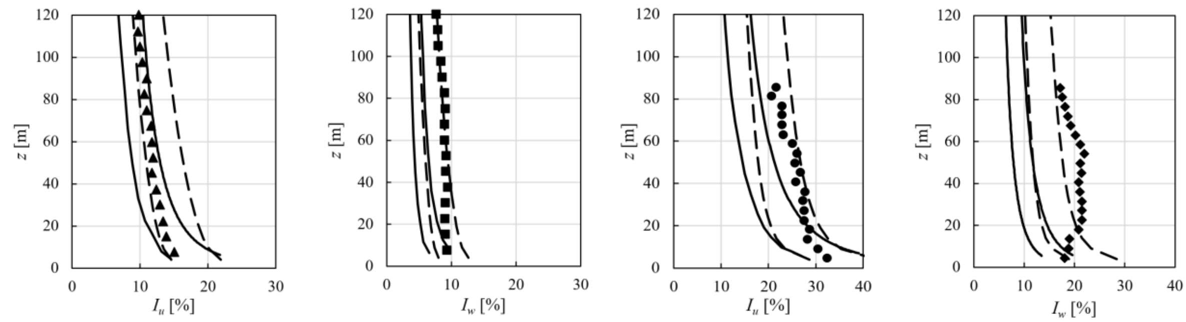

(b) (c) (d) (e)

Figure 6: (a) Longitudinal and vertical turbulence intensity profiles for WTBL1 and WTBL2 in the wind tunnel scale (The shaded area shows the height of the flat plate models in the wind tunnel), (b–c) Full-scale longitudinal and vertical turbulence intensity profiles in 1:151 ABL simulations for WTBL1 compared with ESDU 85020 and ESDU 74031 profiles, (d–e) Full-scale longitudinal and vertical turbulence intensity profiles in 1:90 ABL simulations for WTBL2 compared with ESDU 85020 and ESDU 74031 profiles (The solid and dashed lines show the upper and lower bound of the estimated range from ESDU 74031 and ESDU 85020, respectively).

The longitudinal and vertical power spectral density functions of the two wind tunnel boundary layers, at z=0.3 m, are shown in Figures 7(a) and 7(b), respectively. The non-dimensional power spectral density is compared with the spectra predicted by the theoretical models of von Kármán (1948) which is also recommended by ESDU85020 (2010) to compare the distribution of turbulence energy in the wind tunnel with that at the ASL. The power spectra of both wind tunnel boundary layers show a similar distribution to that of von Kármán which indicates that the turbulence energy distribution in both boundary layers at the model heights is similar to the ASL. Figure 7(b) shows a noticeable shift in the frequency of the peak of the vertical power spectra to higher frequencies. The shift in the peak of power spectra to smaller length scales, which is also reported by Pfahl *et al.* (2015), is due to the different mechanism of turbulence generation in the tunnel compared to the ABL. Furthermore, the larger magnitude of the vertical power spectra for WTBL2 indicates the larger vertical turbulence intensity in the wind tunnel compared to the estimations of the ASL.

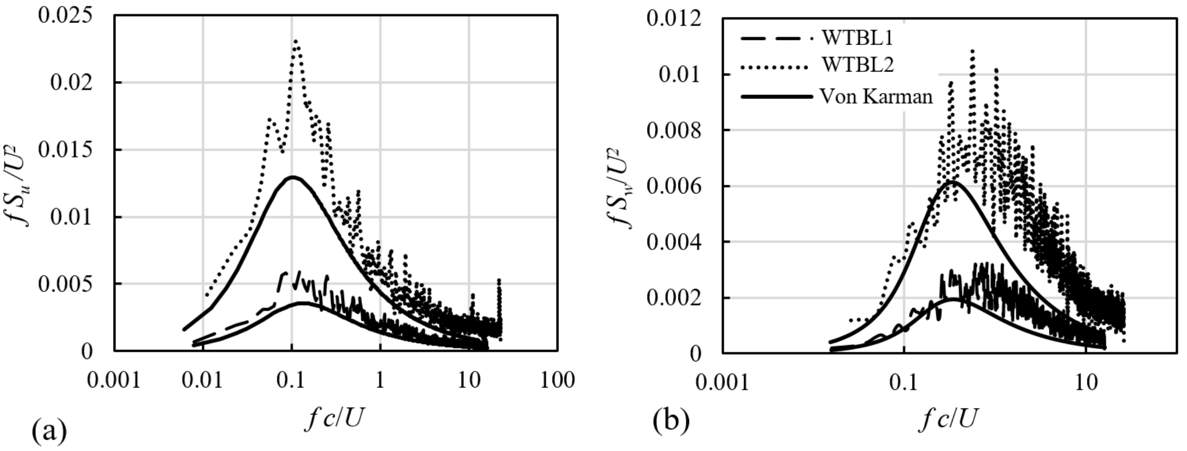

Figure 7: Power spectral density of (a) longitudinal and (b) vertical velocity fluctuation of WTBL1 and WTBL2 as a function of non-dimensional frequency, fc/U, at z=0.3 m, for c=0.5 m (U is the mean velocity at z=0.3 m).

The longitudinal and vertical integral length scales were calculated based on Taylor's hypothesis assuming that the eddies are transported by the mean velocity. In this method, the integral time scale of turbulence is calculated from equation (2) by integration of the auto-correlation of fluctuating longitudinal or vertical velocity components given by equation (3). The length scale is then found by multiplying the integral time scale by the mean velocity as given in equation (4) (Farell and Iyengar, 1999). This method for calculation of integral length scales produces smaller errors compared to other methods, i.e. determination of the value of the spectrum at zero frequency, and semi-empirically from the location of the spectral peak. The former involves significant errors due to lack of adequate resolution at low frequencies (Iyengar and Farell, 2001). Determination of the central peak also leads to errors due to the noise (De Paepe et al., 2016). Therefore, the integral length scales were calculated from the auto-correlation method in this study.

$$\tau_i^x = \int R_i(\tau)d, \quad i = u, w \tag{2}$$

$$R_u(\tau) = \frac{\overline{u'(t)u'(t+\tau)}}{\sigma_u^2} \tag{3}$$

$$L_i^x = \tau_i^x \, U \tag{4}$$

The longitudinal and vertical integral length scales, L_u^x and L_w^x, in the wind tunnel scale for the two boundary layers are shown in Figure 8. There is some scatter in the length scale values which is also reported in the literature (De Paepe *et al.*, 2016; Emes *et al.*, 2018; Kozmar, 2011; Watkins *et al.*, 2006) and is due to limited sampling time and measurement techniques. However, in order to reduce the scatter in the data and to eliminate the error in the determination of the integral length scales, velocity measurements in the wind tunnel were repeated for five times and the average (and standard deviation) of five measurements is reported in Figure 8.

According to Figure 8, the vertical length scale generally decreases as the height in the wind tunnel decreases. In contrast, at heights below 0.2 m, the longitudinal length scale becomes larger as the ground is approached. Above 0.2 m, the longitudinal length scale overall increases as the height from the ground increases. This is due to the turbulence generation technique in the wind tunnel. The spires generate larger turbulence structures close to the ground due to their larger width near the ground. As the height from the ground increases, the width of the spires decreases and smaller turbulence structures are developed. The generated eddies then grow over the longitudinal development length. While at heights below 0.2 m, the development of the eddies is influenced by the ground effect, as the height from the ground further increases, the eddies grow and get larger. The growth and development of the eddies is nevertheless restrained due to the limited cross-section of the wind tunnel as noted in other wind tunnel simulations of the ABL (Banks, 2011; De Paepe *et al.*, 2016; Iyengar and Farell, 2001; Kozmar, 2012; Leitch *et al.*, 2016; Peterka *et al.*, 1998) which reported that the length scales did not increase with height at the same increasing rate observed in the atmosphere. Experimental results in the literature show that the integral length scales in the wind tunnel increase with height but remain almost constant as the height from the ground further increases to reaching towards the ceiling of the tunnel (De Paepe *et al.*, 2016; Iyengar and Farell, 2001; Kozmar, 2011). Unlike the longitudinal length scales, the vertical length scales do not get larger with the increasing width of the spires near the ground since the vertical structures are restrained by the ground. Despite the different mechanism of turbulence generation in the wind tunnel and the atmosphere, the increase in L_u^x and the decrease in L_w^x near the ground is also observed in the lower part of the ASL which is due to the elongation of the turbulent eddies near the ground. In the lower 10 m to 20 m of the ASL, at near-neutral conditions, the eddies, which originate in the lower parts of the middle layer above the surface layer, get stretched and blocked by the ground as they impinge upon it. Consequently, the vertical velocity tends to zero near the ground (Högström *et al.*, 2002; Hunt and Carlotti, 2001).

According to Figure 8, the longitudinal and vertical integral length scales in WTBL2 are larger than those for the WTBL1. The longitudinal integral length scales at the heliostat positions are between 0.66 m to 0.75 m for WTBL2, while they are about 0.52 m to 0.67 m for WTBL1. According to Figure 8, the vertical length scales at the heliostat positions are between 0.2 m to 0.25 m for WTBL1 and between 0.27 m to 0.35 m for WTBL2. Therefore, the flat plate models can be exposed to different scales of turbulence within the two simulated boundary layers which allows investigation of the effect of the relative size of the integral length scale to the chord length on the loads. Figure 8(b–e) show the longitudinal and vertical integral length scales within the two wind tunnel boundary layers converted to full scale in comparison with the recommended ESDU 74031 and ESDU 85020 ranges for the corresponding open country and suburban terrains. The integral length scales are in general within the ranges predicted by ESDU 85020 and ESDU 74031.

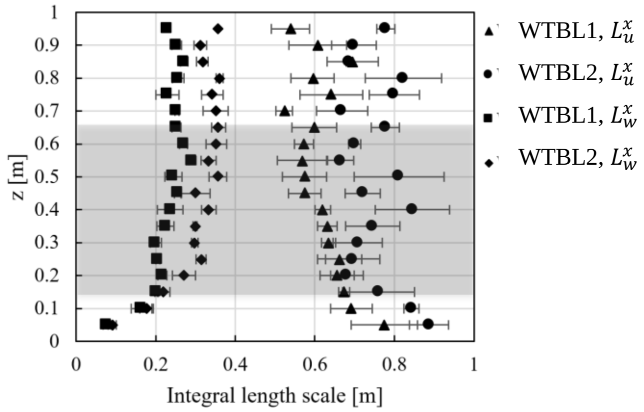

(a)

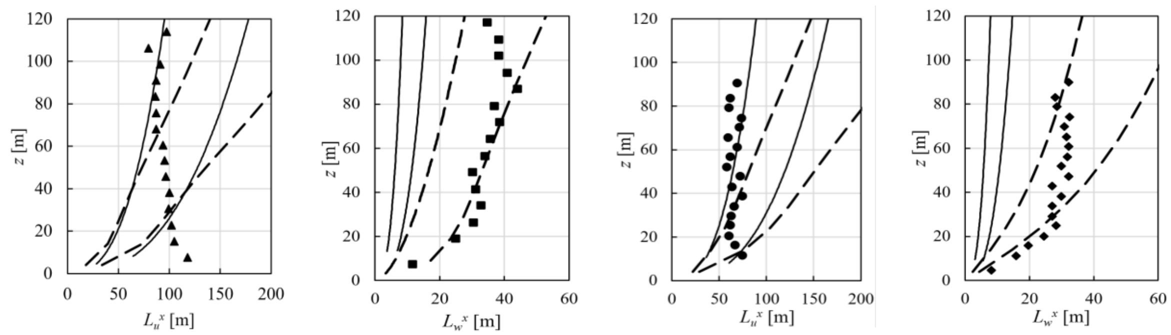

(b) (c) (d) (e)

Figure 8: (a) Longitudinal and vertical integral length scales for WTBL1 and WTBL2 in the wind tunnel scale (The error bars show the standard deviation calculated from five measurements), (b-c) Full-scale longitudinal and vertical integral length scales in 1:151 ABL simulations for WTBL1 compared with ESDU 85020 and ESDU 74031 profiles, (d-e) Full-scale longitudinal and vertical integral length scales in 1:90 ABL simulations for WTBL2 compared with ESDU 85020 and ESDU 74031 profiles (The solid and dashed lines show the upper and lower bound of the estimated range from ESDU 74031 and ESDU 85020, respectively).

A summary of the velocity and turbulence characteristics of the two wind tunnel boundary layers is given in Table 1.

Table 1 Summary of the characteristics of the two wind tunnel boundary layers (the turbulence intensity and length scales are given for the heights of the heliostat models). The aerodynamic surface roughness and the integral length scale are given in model scale.

	Length scale factor	z_0**(mm)**	I_u**(%)**	I_w**(%)**	L_u^x **(m)**	L_w^x **(m)**
WTBL1	1:151	0.12	11	9	0.52–0.67	0.2–0.25
WTBL2	1:90	3.88	26	19	0.66–0.75	0.27–0.35

3 Results

In order to find the effect turbulence characteristics on the wind loads, forces on horizontal flat plate models with varying pylon heights (with H/c ratios between 0.2 and 1.3) were measured. The measurements were undertaken at longitudinal turbulence intensities of approximately 11% and 26% and vertical turbulence intensities of approximately 9% and 21% produced within the wind tunnel boundary layers using the two spire sets. Furthermore, three square plates with chord length dimensions of 0.5, 0.6 and 0.7 m were used to achieve different ratios of L_u^x/c and L_w^x/c. Figure 9 shows the variations of the peak lift force coefficient on the horizontal flat plates with changing the flat plate heights as a function of H/c. It is found that $C_{L,p}$ decreases linearly with reducing H/c, which agrees with the results reported by Emes et al. (2017) who found a similar trend for the peak lift force coefficient on stowed heliostats for H/c values between 0.5 and 1.3. The results reported by Emes et al. (2017) were limited to H/c=0.5 and lower turbulence intensity (I_u=6–12.5%). The results of the present study shown in Figure 9 indicate that $C_{L,p}$ on a stowed heliostat is further reduced by decreasing H/c to below 0.5. According to Figure 9, reducing H/c from 0.5 to 0.2 reduces $C_{L,p}$ from approximately 0.3 to 0.2 at an average vertical turbulence intensity of 9%, and from 0.65 to 0.48 at an average vertical turbulence intensity of 19%. Furthermore, as shown in Figure 9, the rate of reduction of $C_{L,p}$ with reducing H/c is larger in WTBL2, where the turbulence intensity and integral length scales are larger than those in WTBL1, such that the slope of the linear trend for WTBL2 is three times larger than WTBL1 ($\frac{dC_{L,p}}{d(H/c)}$=0.18 and 0.67 for WTBL1 and WTBL2, respectively).

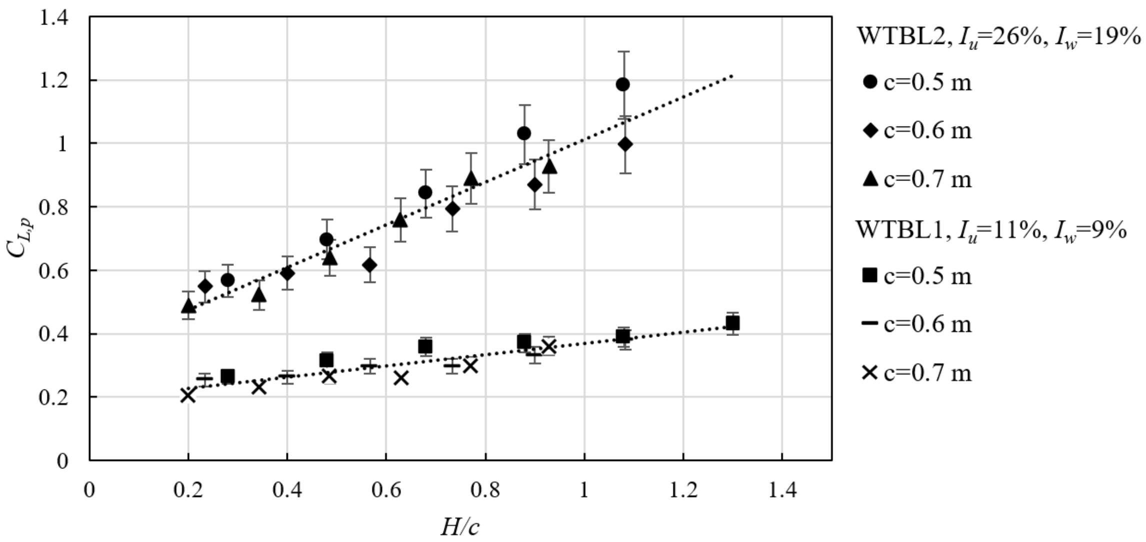

Figure 9: The effect of height to chord length ratio, H/c, on the peak lift force coefficient on a horizontal flat plate, $C_{L,p}$, for WTBL1, $I_u = 11\%$ and $I_w = 9\%$, and WTBL2, $I_u = 26\%$ and $I_w = 19\%$.

Reduction of the peak lift force coefficient with the reduction of the height of the flat plate shown in Figure 9 is due to the effect of turbulence. As the height of each flat plate within each boundary layer is reduced from 0.64 m to 0.14 m, it is exposed to a different turbulence condition. According to Figure 6 and as shown in Table 1, longitudinal and vertical turbulence intensity remain almost constant (varying by less than 2%) over the range of heights between 0.14 m and 0.64 m. Therefore, the reduction of $C_{L,p}$ with height for each plate in each boundary layer is not related to turbulence intensity. On the other hand, the integral length scales of turbulence vary with height in each boundary layer. Therefore, the reduction of $C_{L,p}$ is due to the effect of the integral length scale of turbulence. According to Figure 8, as the height reduces from 0.64 m to 0.14 m in each boundary layer, L_w^x decreases while L_u^x does not consistently decrease and increases at some heights. Hence, reduction of $C_{L,p}$ for a single flat plate (constant c) as H reduces is due to the reduction of L_w^x. The effect of L_w^x on the peak lift force coefficient is shown in Figure 10, which presents the change in the peak lift force coefficient as a function of L_w^x/c, for each flat plate (constant chord length dimension) as the height of the pylon changes. As the height of the plates from the ground reduces, the vertical length scales and consequently L_w^x/c for each plate size decrease, which results in the reduction of the peak lift force coefficient as shown in Figure 10. For instance, reducing L_w^x/c from 0.7 to 0.54 reduces the peak lift force coefficient from approximately 1.18 to 0.57 for c=0.5 m and I_w =19%. Similarly, $C_{L,p}$ reduces from 0.43 to 0.26 by reducing L_w^x/c from 0.51 to 0.43 for c=0.5 m and I_w =9%. The results in Figure 10 show that $C_{L,p}$ increases as a power function of L_w^x/c, with an exponent between 2.2 and 2.5.

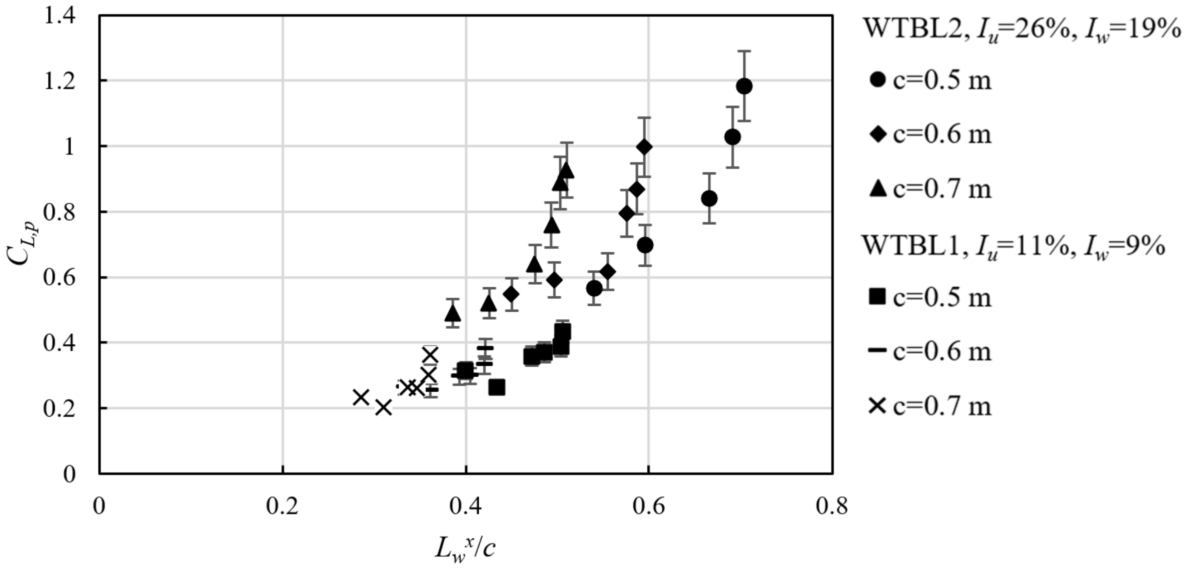

Figure 10: The effect of vertical integral length scale to chord length ratio, L_w^x/c, on the peak lift force coefficient, $C_{L,p}$, on a horizontal flat plate within WTBL1, I_w =19%, and WTBL2, I_w =9%.

As the height within the simulated boundary layers decreases, the vertical velocity component is reduced due to the no-slip effect of the ground. According to Figure 8, with the decrease of the height within the boundary layer, L_w^x decreases and the vertical to longitudinal length scale ratio, L_w^x/L_u^x reduces, which represents how the eddies are more elongated in the longitudinal direction at the lower heights near the ground resulting in smaller magnitude of the vertical velocity component. As the eddy hits the plate, the vertical velocity component, which is normal to the flat plate, produces the vertical lift force by generating pressure and suction on the plate surface. L_w^x represents the longitudinal distance over which the vertical velocity components are well correlated. L_w^x/c is indicative of the extent to which the eddies engulf the plate. Therefore, less lift is produced on larger plates with smaller L_w^x/c since a smaller area of the plate is impacted by the vertical velocity component of the eddy. Therefore, the reduction of the vertical length scales at lower heights close to the ground leads to the reduction of the fluctuating component of the lift force coefficient.

Emes *et al.* (2017) proposed that the peak lift force coefficient on a stowed heliostat increases linearly with L_u^x/c. The trend reported by Emes *et al.* (2017) was achieved by measuring the lift force coefficient on flat plates of different chord length dimensions at a constant height and constant L_u^x and L_w^x. The ratio of L_u^x/c was varied by changing only c while L_u^x was constant. While c increased, both L_u^x/c and L_w^x/c decreased. However, the effect of variation of L_w^x/c was not taken into account. Therefore, the reported results by Emes *et al.* (2017) were simultaneously affected by both longitudinal and vertical turbulence length scales. The method used in the present study is different from Emes *et al.* (2017) as the effect of integral length scale is investigated by exposing a single flat plate with a constant c to different turbulence length scales by changing the height of the plate in the boundary layer. To achieve a larger set of data, flat plates of different dimensions were used in two boundary layers. In the results of the present study shown in Figure 10, L_u^x and L_w^x are varied for a constant value of c by changing the height of each plate in the two boundary layers. Although both L_u^x/c and L_w^x/c are varied in the current experiments, the results show that $C_{L,p}$ is more strongly correlated with L_w^x/c (Figure 10). Therefore, the vertical integral length scale, L_w^x, is the major contributor to the lift force on the horizontal flat plate, not L_u^x. This is further supported by comparison of $C_{L,p}$ for cases with similar L_u^x/c and different L_w^x/c, as presented in Figure 11. For instance, the peak lift force coefficient increases from 0.62 to 1.18 as L_w^x/c increases from 0.55 to 0.7 although L_u^x/c remains constant at approximately 1.4. Another example is increase of $C_{L,p}$ from approximately 0.54 to 0.99 when L_w^x/c increases from 0.45 to 0.59 at L_u^x/c=1.1. Hence, the results show that the peak lift force coefficient increases with increasing L_w^x/c.

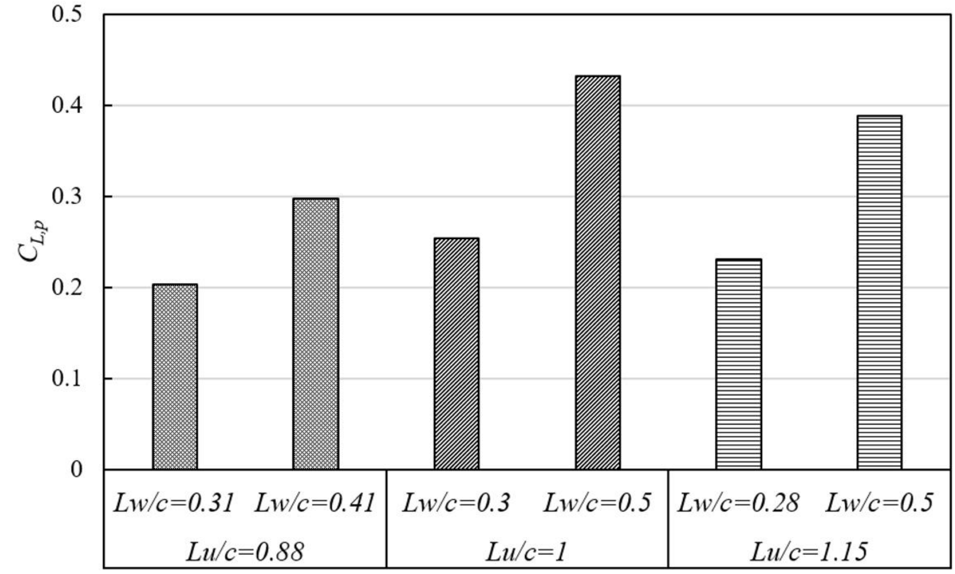

(a)

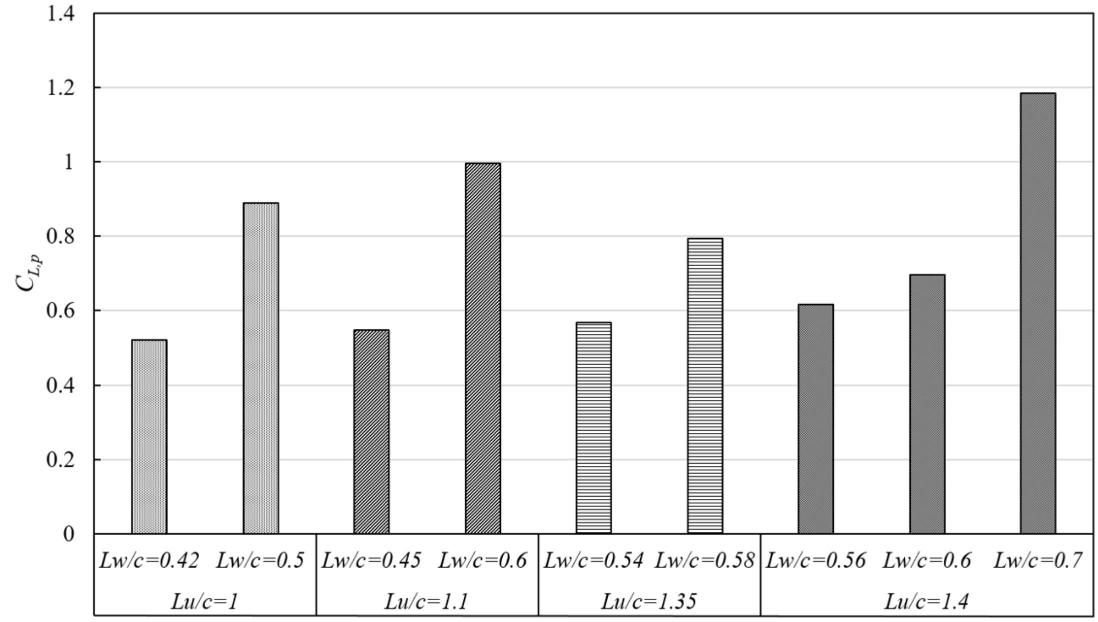

(b)

Figure 11: Comparison of the peak lift force coefficient for cases with similar L_u^x/c and different L_w^x/c, (a) WTBL1, I_u =11% and I_w =19%, (b) WTBL2, I_u =26% and I_w =21%.

The dependency of the fluctuating lift force on the fluctuating vertical velocity component found in the present study is in agreement with that reported by (Larose and Livesey, 1997; Pfahl, 2018; Rasmussen *et al.*, 2010). Assuming quasi-steady aerodynamics, the lift force coefficient can be defined as a linear function of the angle of attack (φ) (Rasmussen *et al.*, 2010),

$$C_L(\varphi) = C_{L,0}(\varphi = 0) + \frac{\partial C_L}{\partial \varphi}\varphi \tag{5}$$

where the instantaneous angle of attack is given by $\varphi = \frac{w}{U+u'}$. Rasmussen *et al.* (2010) shows that the lift force on a horizontal flat plate caused by the fluctuating wind can be expressed as,

$$F_L = \frac{\rho U A}{2}(2C_{L,0}u' + \frac{\partial C_L}{\partial \varphi}w') \tag{6}$$

where $C_{L,0}$ and $\frac{\partial C_L}{\partial \varphi}$ represent the lift force coefficient at $\varphi = 0$ and the slope of the lift force coefficient at near zero angle of attack, respectively. $C_{L,0}$ and $\frac{\partial C_L}{\partial \varphi}$ can be determined through static tests by measuring the lift force on flat plates at small elevation angles according to the method given by Cigada *et al.* (2002), and were measured to be equal to -0.11 and 2.90 respectively. The experimental values of $C_{L,0} = -0.11$ and $\frac{\partial C_L}{\partial \varphi}$=2.9 are in agreement with those reported for bridge decks (Larose *et al.*, 1998) showing that $\frac{\partial C_L}{\partial \varphi}$ is much larger compared to

$C_{L,0}$. Based on Equation (6) and since $\frac{\partial C_L}{\partial \varphi}$ is much larger in magnitude compared to $C_{L,0}$, the lift force is mainly influenced by the vertical velocity component.

The effect of vertical turbulence intensity can also be seen in Figure 10, as at similar values of L_w^x/c, $C_{L,p}$ is larger for the WTBL2 where the turbulence intensity is larger. For example, at L_w^x/c=0.5, $C_{L,p}$ equals approximately 0.43 and 0.6 for I_w =9% and I_w =19%, respectively. Therefore, the peak lift force coefficient is a function of both integral length scale and turbulence intensity. This relationship can be expressed in terms of the turbulence parameter represented by $\eta = I_w(\frac{L_w^x}{c})^{2.4}$. Similar parameters defined by longitudinal turbulence intensity and length scale have been correlated with the pressure coefficient on a flat plate normal to the flow in terms of $I_u(\frac{L_u^x}{c})^2$ by Bearman (1971), and a thick blunt horizontal plate as $I_u(\frac{L_u^x}{c})^{0.15}$ by Li and Melbourne (1995) in which the flow is different from the case of a thin horizontal flat plate in an atmospheric boundary layer flow. As described earlier, the fluctuating lift force on the flat plate is induced by the vertical velocity component resulting from the variations in the angle of attack of the flow induced by the turbulent eddies (see Equation 6). The turbulence parameter is calculated for the three chord length dimensions (c=0.5, 0.6, 0.7 m) of the plates within WTBL1 and WTBL2 and the investigated H/c ratios between 0.2 and 1.3. For the flat plate in a boundary layer flow, the current experimental data suggest the best fit for $C_{L,p}$ is achieved for $\eta = I_w(\frac{L_w^x}{c})^{2.4}$. Figure 12 shows the peak lift force coefficient as a function of η. According to Figure 12, $C_{L,p}$ increases logarithmically with the turbulence parameter, which can be described by the following correlation:

$$C_{L,p} = 0.267\ln(\eta) + 1.566 \tag{7}$$

This finding is in agreement with that found by Bearman (1971) reporting that the pressure coefficient on a plate normal to the turbulent flow increases logarithmically with the turbulence parameter, $I_u(\frac{L_u^x}{c})^2$. The turbulence parameter can be interpreted as an expression of the entrainment of the turbulence energy (Bearman, 1971). The dependency of the lift force on the turbulence parameter indicates that the force is the result of both spatial and temporal coherence of vertical turbulence energy. The determined relationship in terms of the turbulence parameter indicates that the peak lift force coefficient is more sensitive to L_w^x/c than to turbulence intensity, I_w. Therefore, the effect of the spatial distribution of vertical turbulence energy on the peak lift force coefficient on a stowed heliostat is more significant than the temporal release of turbulent energy.

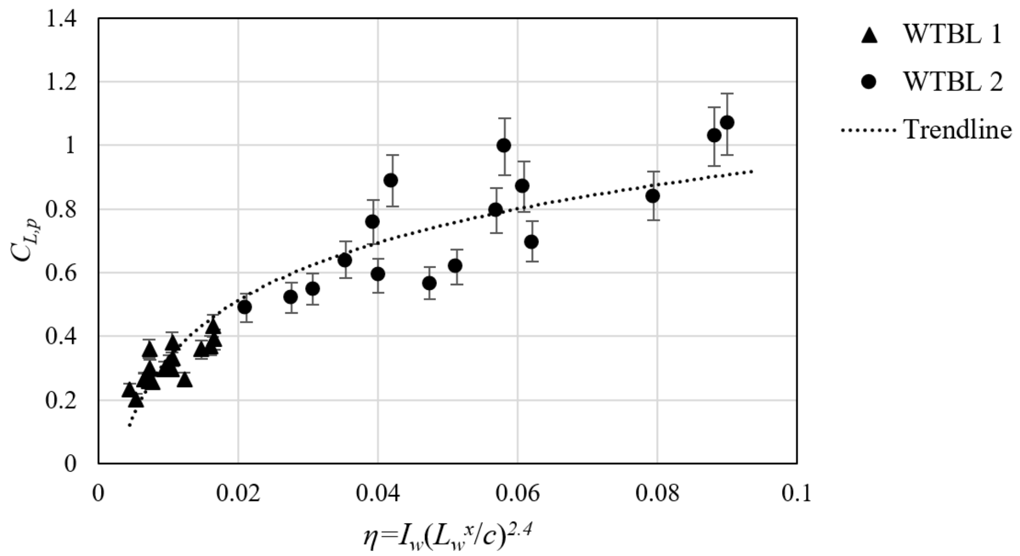

Figure 12: Variations of the peak lift force coefficient on horizontal flat plates, $C_{L,p}$, with the turbulence parameter, η.

4 Case study: Lift force on stowed heliostats

The results presented in the previous section indicate that the effect of free-stream turbulence on the peak lift force coefficient on a thin horizontal flat plate is predominantly affected by the turbulence parameter. In this section, the correlation between the lift force and the turbulence parameter developed from the wind tunnel experiments is used to predict the lift force on stowed heliostats as a case study. Heliostats with square mirror panels with a chord length dimension between 2 m and 10 m, and with pylon heights between 0.2 c and 0.5 c are considered. First, the turbulence parameter for the heliostats within ASL is calculated from equation $\eta = I_w (\frac{L_w^x}{c})^{2.4}$ using estimations of the integral length scales and turbulence intensity at terrains with different surface roughness values. Then the lift force coefficient is predicted as a function of the turbulence parameter from Equation (7).

To estimate the turbulence parameter for heliostats within the ASL, the vertical turbulence intensity and integral length scale were calculated for different terrain roughness values and heights within the ASL using the empirical relationships given by ESDU85020 (2010), and are given in Figure 13(a). The turbulence parameter was then calculated for heliostats with chord lengths of the mirror panel between 2 m to 10 m and for different pylon heights, from the equation, $= I_w (\frac{L_w^x}{c})^{2.4}$, using the turbulence intensity and length scales corresponding to each height. An example of the calculations is given in Table 2 for a terrain roughness of 0.1 m. Similar calculations were carried out for different surface roughness values between 0.01 m and 0.3 m. The results showed that the turbulence parameters for heliostats with different pylon heights and chord length dimensions of the panel, which have an identical H/c, are similar and can be expressed as a single value with a maximum standard deviation of 15%. Therefore, the average value of the turbulence parameter can be given for heliostats of constant H/c ratio at each terrain roughness, and the turbulence can be expressed as a function of terrain roughness and H/c, i.e. $\eta = f(z_0, \frac{H}{c})$. This is due to the dependence of the turbulence intensity and length scale on height and the relationship between the height and chord length of the mirror panel of heliostats. The turbulence parameter for different roughness values (z_0 =0.01 m to 0.3 m) as a function of H/c is shown in Figure 13(b). The error bars in Figure 13(b) show the standard deviation from the average values for a specific H/c. According to Figure 13(b), the turbulence parameter is larger for smaller values of surface roughness. For instance, at H/c=0.5, the turbulence parameter increases from approximately 0.016 to 0.054 when the surface roughness decreases from 0.3 m to 0.01 m. This is because the vertical integral length scales tend to decrease with increase in surface roughness at heights below 10 m where heliostats are positioned within the ASL, according to ESDU85020 (2010). Furthermore, according to Figure 13(b), at a specific terrain, the turbulence parameter increases with a power function with increasing H/c. Decreasing H/c from 0.5 to 0.2 leads to a reduction of the turbulence parameter to below 0.01 for the considered range of surface roughness values. It must be mentioned that the values of the turbulence parameter within the ABL shown in Figure 13 are calculated for heights above 3 m since the relationships for integral length scale and turbulence intensity given by ESDU85020 (2010) hold true for a minimum height of 3 m.

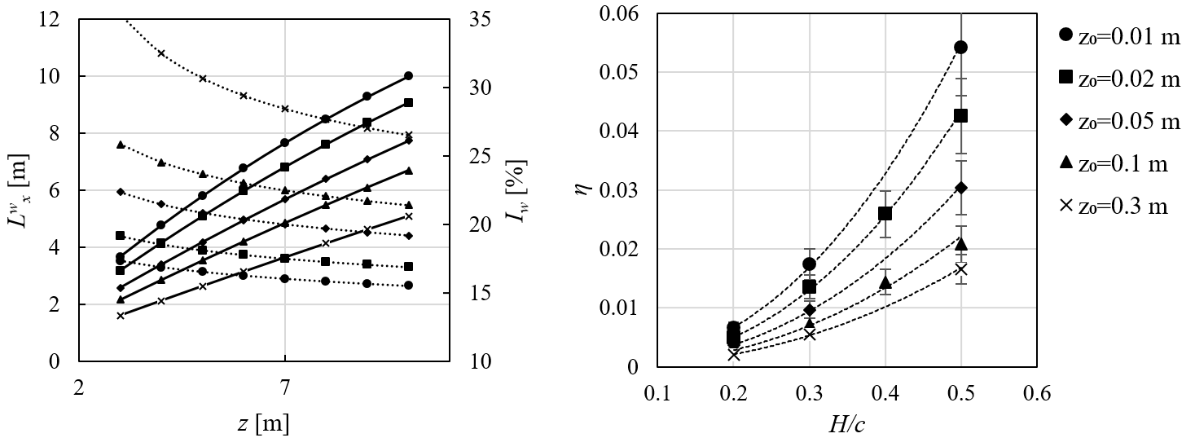

(a) (b)

Figure 13: (a) Vertical length scale (solid lines) and turbulence intensity (dotted lines) within the ASL calculated from ESDU85020 (2010) in full-scale (b) The turbulence parameter, η, within the ASL as a function of terrain roughness, z_0, and hinge height to chord length ratio of heliostats, H/c.

Table 2: Estimations of the vertical turbulence intensity, vertical length scale and the turbulence parameter for heliostats with different chord length dimensions of the mirror panel and pylon heights for a terrain with z_0=0.1 m in full-scale

$\boldsymbol{H}$ [m]	$\boldsymbol{I_w}$ [%]	$\boldsymbol{L_w^x}$ [m]	$\boldsymbol{c}$ [m]	$\boldsymbol{H/c}$	$\boldsymbol{L_w^x/c}$	$\boldsymbol{\eta}$
3	25.83	2.164	6	0.5	0.360	0.022
3	25.83	2.164	7.5	0.4	0.288	0.013
3	25.83	2.164	10	0.3	0.216	0.006
4	24.53	2.859	8	0.5	0.357	0.021
4	24.53	2.859	10	0.4	0.285	0.012
4	24.53	2.859	13.3	0.3	0.215	0.006

According to Figure 13(b), for industrial-scale heliostats within the ABL with terrain roughness values between 0.01 m and 0.3 m the turbulence parameter is between 0.005 and 0.054. The peak lift force coefficient on full-scale heliostats within the ABL can then be predicted based on the relationship given by Equation (7). According to Equation (7), as the turbulence parameter increases from 0.005 to 0.054, the peak lift force coefficient on a stowed heliostat increases from 0.146 to 0.787.

As mentioned in the previous sections, heliostats and solar trackers are conventionally designed H/c of about 0.5 (Téllez *et al.*, 2014). According to Emes *et al.* (2017) the lift force coefficient on a stowed heliostat model, in a wind tunnel boundary layer with a longitudinal turbulence intensity of 6%, decreases by about 80% when H/c from 1.2 to 0.5. Therefore, there seems to be a potential to decrease wind loads at stow position by further reducing H/c. In order to assess this potential, the turbulence parameter for full-scale heliostats within the ASL with different height to chord length ratios are calculated from ESDU85020 (2010) and thereafter, the lift force coefficient is found as a function of the turbulence parameter by Equation (7). The corresponding values of the turbulence parameter and the peak lift force coefficient for H/c ratios between 0.2 and 0.5 are presented in Table 3 for surface roughness values of 0.02 m and 0.1 m as samples of two terrain types. According to Table 3, reducing H/c from 0.5 to 0.2 for a stowed heliostat in a terrain with a surface roughness of 0.02 m, leads to a reduction in turbulence parameter from approximately 0.042 to 0.004 which decreases the $C_{L,p}$ from 0.722 to 0.146. Similarly, stowing at H/c=0.2 instead of H/c=0.5 reduces the peak lift force coefficient from 0.531 to 0.068 at z_0 =0.1 m. The last row in Table 3 shows the peak lift force coefficient normalised with that at H/c=0.5, $C_{L,p(0.5)}$, which is chosen for normalising the lift force coefficient since heliostats are usually designed for H/c=0.5.

Table 3: The turbulence parameter within the full-scale ASL for different surface roughness values and stow H/c ratios and its effect on the peak lift force coefficient on a full-scale stowed heliostat

	$\boldsymbol{z_0 = 0.02}$ **m**				$\boldsymbol{z_0 = 0.1}$ **m**			
$\boldsymbol{H/c}$	0.5	0.4	0.3	0.2	0.5	0.4	0.3	0.2
η	0.042	0.025	0.013	0.004	0.020	0.014	0.007	0.003
$\boldsymbol{C_{L,p}}$	0.722	0.590	0.417	0.146	0.531	0.433	0.249	0.068
$\boldsymbol{C_{L,p}/C_{L,p(0.5)}}$	1	0.816	0.577	0.202	1	0.815	0.468	0.108

The normalised peak lift force coefficient as a function of H/c is shown in Figure 14 for different terrain roughness values and H/c between 0.2 and 0.8. According to Figure 14, the normalised peak lift force coefficient on stowed heliostats within the ASL is a linear function of H/c, nearly independent of the terrain roughness. This relationship indicates that decreasing H/c from 0.5 to 0.2 reduces the peak lift force coefficient on stowed heliostats by 80% for all of the terrain types.

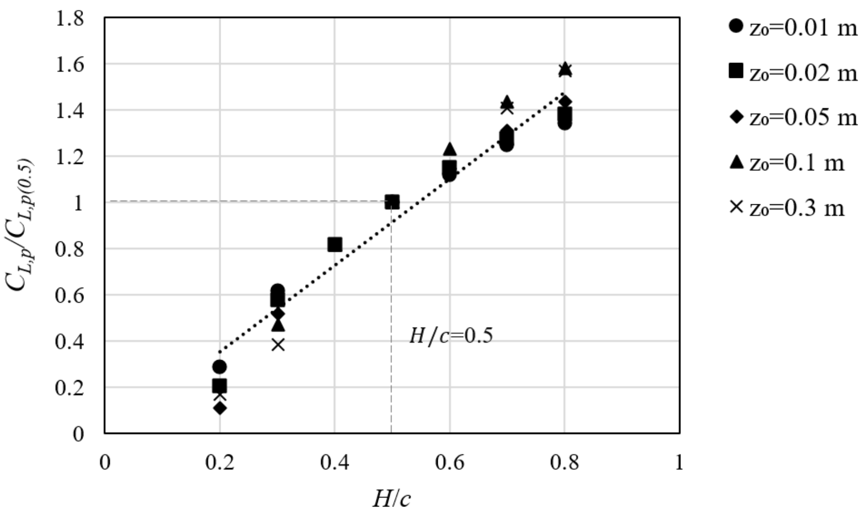

Figure 14: The peak lift force coefficient, $C_{L,p}$, of a full-scale stowed heliostat within the ASL normalised with that for H/c=0.5, $C_{L,p(0.5)}$, as a function of heliostat hinge height to chord length ratio, H/c.

The results presented in this section show that the turbulence parameter and the peak lift force coefficient on stowed heliostats depend on H/c and are the same for heliostats of various chord lengths with a similar H/c ratio. Although the peak lift force coefficient is the same for heliostats of different sizes with an identical H/c, the lift force is larger on heliostats with larger chord length of the mirror panel due to the larger panel area. Therefore, peak wind loads at stow position can be reduced by stowing heliostats at lower H/c ratios and by reducing the panel area.

Furthermore, it is noteworthy that the values of turbulence parameter given in Figure 13 are calculated for a single heliostat and therefore apply to heliostats in the outermost row of a field exposed to the wind. Mean wind loads on the heliostats in the inner rows of a field are less than the first row due to the shielding effect of the first row (Peterka, Bienkiewicz, *et al.*, 1987; Pfahl, 2011). Therefore, use of a first row of heliostats as a buffer has been proposed. However, heliostats placed within a field are exposed to different scales and intensities of turbulence. The dominant frequency of the fluctuating pressure on a second tandem heliostat in stow is an order of magnitude smaller than that for a single heliostat which indicates that the upstream heliostat breaks up the large energetic eddies within the flow (Emes *et al.*, 2018). Furthermore, turbulence intensity is found to increase dramatically after the second row of heliostats (Sment and Ho, 2014). The dynamic loads are dependent on the turbulence characteristics among the rows of heliostats. Therefore, it is necessary to investigate turbulence characteristics and wind loads for heliostats placed within rows of a field in future studies.

5 Conclusion

The effect of turbulence intensity and length scales on the peak lift force on a horizontal flat plate in a longitudinal turbulent flow was investigated in this study. Comprehensive experimental investigations were conducted to measure the wind loads on flat plate models at various heights within a part-depth wind tunnel model of the atmospheric surface layer. The following conclusions were reached from the obtained results:

- The peak lift force coefficient on a horizontal flat plate in an atmospheric boundary layer flow increases as a power function, with an exponent between 2.2 and 2.5, of the ratio of vertical integral length scale to the chord length of the plate.
- The peak lift force coefficient on a horizontal flat plate increases with increasing the vertical turbulence intensity.
- Turbulence parameter, which expresses the effect of both vertical turbulence intensity and vertical integral length scales, is the key factor affecting the peak lift force coefficient on horizontal flat plates, such that the peak lift force coefficient increases logarithmically with the turbulence parameter.

The developed correlation between the peak lift force coefficient and the turbulence parameter was used to predict the wind loads on stowed heliostats with square mirror panels as a case study. The results showed that:

- The turbulence parameter for heliostats with a chord length dimension below 10 m is between 0.005 and 0.054 for z_0=0.01 m to 0.3 m and can be expressed as a function of terrain roughness and heliostat height to chord length ratio.
- The peak lift force coefficient on stowed heliostats can be expressed as a linear function of the pylon height to chord length ratio of a heliostat. Its value is identical for heliostats regardless of the mirror panel chord length as long as H/c is the same, but it is dependent on the terrain roughness.
- Reducing H/c at stow position from 0.5 to 0.2 decreases the peak lift force coefficient on stowed heliostats by approximately 80%, independent of the terrain roughness.

Hence, the results of this study show that decreasing the heliostat height and thereby height to chord length ratio at stow position leads to reduction of the peak lift force at stow. It is recommended to stow heliostats at lower H/c ratios by adjustment of the pylon design, as for instance, lowering H/c to 0.2 or 0.3 will lead to a reduction of the peak lift force coefficient and thereby the lift force by approximately 50% and 80%, accordingly, for all terrain surface roughness values. Therefore, there is a great potential for reduction of the cost of heliostats since the overall required mass and strength of the structure can be decreased. This can be achieved by design of telescopic pylons with adjustable height to allow heliostats to be stowed at lower heights while operating at larger H/c values. An example of a heliostat design with adjustable height is the DLR carousel heliostat in which the panel is lowered to the ground during stow (Pfahl *et al.*, 2017). In order to provide an estimation of the potential cost reduction, it is necessary to further investigate the cost of the new pylon design in the future studies. Furthermore, investigation of the hinge and overturning moments at stow position is required since they must be considered for the survivability of the structure, and they are dependent on the centre of pressure in addition to the lift force. Moreover, comparison of the wind tunnel results with measurements of wind loads on full-scale heliostats will be done in future.

Acknowledgements

Financial support for the project has been provided by the Australian Government Research Training Program, the University of Adelaide Scholarship and the Australian Solar Thermal Research Initiative (ASTRI). The authors would like to acknowledge the School of Mechanical Engineering and the workshop at the University of Adelaide.

References

Banks, D. 2011. Measuring peak wind loads on solar power assemblies. In *13th International Conference on Wind Engineering*. Amsterdam, Netherlands.

Bearman, P. W. 1971. An investigation of the forces on flat plates normal to a turbulent flow, *Journal of Fluid Mechanics*, 46: 177-98.

Bearman, P. W., and Morel, T. 1983. Effect of free stream turbulence on the flow around bluff bodies, *Progress in Aerospace Sciences*, 20: 97-123.

Cigada, A., Diana, G., and Zappa, E. 2002. On the response of a bridge deck to turbulent wind: a new approach, *Journal of Wind Engineering and Industrial Aerodynamics*, 90: 1173-82.

Cook, N. J. 1978. Determination of the model scale factor in wind-tunnel simulations of the adiabatic atmospheric boundary layer, *Journal of Wind Engineering and Industrial Aerodynamics*, 2: 311-21.

De Paepe, W., Pindado, S., Bram, S., and Contino, F. 2016. Simplified elements for wind-tunnel measurements with type-III-terrain atmospheric boundary layer, *Measurement*, 91: 590-600.

Emes, M. J., Arjomandi, M., Ghanadi, F., and Kelso, R. M. 2017. Effect of turbulence characteristics in the atmospheric surface layer on the peak wind loads on heliostats in stow position, *Solar Energy*, 157: 284-97.

Emes, M. J., Ghanadi, F., Arjomandi, M., and Kelso, R. M. 2018. Investigation of peak wind loads on tandem heliostats in stow position, *Renewable Energy*, 121: 548-58.

ESDU74031. 1974. Characteristics of atmospheric turbulence near the ground - Part II: single point data for strong winds (neutral atmosphere), *Engineering Sciences Data Unit*.

ESDU85020. 2010. Characteristics of atmospheric turbulence near the ground - Part II: single point data for strong winds (neutral atmosphere), *Engineering Sciences Data Unit*.

Farell, C., and Iyengar, A. K. S. 1999. Experiments on the wind tunnel simulation of atmospheric boundary layers, *Journal of Wind Engineering and Industrial Aerodynamics*, 79: 11-35.

Gong, B., Wang, Z., Li, Z., Zang, C., and Wu, Z. 2013. Fluctuating wind pressure characteristics of heliostats, *Renewable Energy*, 50: 307-16.

Högström, U., Hunt, J. C. R., and Smedman, A.-S. 2002. Theory and measurements for turbulence spectra and variances in the atmospheric neutral surface layer, *Boundary-Layer Meteorology*, 103: 101-24.

Holdø, A. E., Houghton, E. L., and Bhinder, F. S. 1982. Some effects due to variations in turbulence integral length scales on the pressure distribution on wind-tunnel models of low-rise buildings, *Journal of Wind Engineering and Industrial Aerodynamics*, 10: 103-15.

Holmes, J. D. 2007. *Wind Loading of Structures*, Taylor & Francis.

Hunt, J. C. R., and Carlotti, P. 2001. Statistical structure at the wall of the high Reynolds number turbulent boundary layer, *Flow, Turbulence and Combustion*, 66: 453-75.

Irwin, H. P. A. H. 1981. The design of spires for wind simulation, *Journal of Wind Engineering and Industrial Aerodynamics*, 7: 361-66.

Iyengar, A. K. S., and Farell, C. 2001. Experimental issues in atmospheric boundary layer simulations: Roughness length and integral length scale determination, *Journal of Wind Engineering and Industrial Aerodynamics*, 89: 1059-80.

Jafari, A., Emes, M. J., Ghanadi, F., and Arjomandi, M. 2017. The effect of turbulence intensity on the peak wind loads on heliostats. In *The Asia Pacific Solar Research Conference 2017*. Melbourne, Australia.

Kozmar, H. 2011. Truncated vortex generators for part-depth wind-tunnel simulations of the atmospheric boundary layer flow, *Journal of Wind Engineering and Industrial Aerodynamics*, 99: 130-36.

Kozmar, H. 2011. Wind-tunnel simulations of the suburban ABL and comparison with international standards, *Wind and Structures*, 14: 15-34.

Kozmar, H. 2012. Physical modeling of complex airflows developing above rural terrains, *Environmental Fluid Mechanics*, 12: 209-25.

Larose, G. L., and Livesey, F. M. 1997. Performance of streamlined bridge decks in relation to the aerodynamics of a flat plate, *Journal of Wind Engineering and Industrial Aerodynamics*, 69-71: 851-60.

Larose, G. L., Tanaka, H., Gimsing, N. J., and Dyrbye, C. 1998. Direct measurements of buffeting wind forces on bridge decks, *Journal of Wind Engineering and Industrial Aerodynamics*, 74-76: 809-18.

Leitch, C. J., Ginger, J., and Holmes, J. 2016. Wind loads on solar panels mounted parallel to pitched roofs, and acting on the underlying roof, *Wind and Structures*, 22: 307-28.

Li, Q. S., and Melbourne, W. H. 1995. An experimental investigation of the effects of free-stream turbulence on streamwise surface pressures in separated and reattaching flows, *Journal of Wind Engineering and Industrial Aerodynamics*, 54-55: 313-23.

Li, Q. S., and Melbourne, W. H. 1999. The effect of large-scale turbulence on pressure fluctuations in separated and reattaching flows, *Journal of Wind Engineering and Industrial Aerodynamics*, 83: 159-69.

Peterka, J. A., Bienkiewicz, B., Hosoya, N., and Cermak, J. E. 1987. Heliostat mean wind load reduction, *Energy*, 12: 261-67.

Peterka, J. A., Hosoya, N., Dodge, S., Cochran, L., and Cermak, J. E. 1998. Area-average peak pressures in a gable roof vortex region, *Journal of Wind Engineering and Industrial Aerodynamics*, 77-78: 205-15.

Peterka, J. A., Tan, L., Bienkiewcz, B., and Cermak, J. E. 1987. Mean and peak wind load reduction on heliostats, *Technical Report for Colorado State University*.

Peterka, J. A., Tan, Z., Cermak, J. E., and Bienkiewicz, B. 1989. Mean and peak wind loads on heliostats, *Journal of Solar Energy Engineering*, 111: 158-64.

Pfahl, A. 2018. Wind loads on heliostats and photovoltaic trackers, *Eindhoven: Technische Universiteit Eindhoven*.

Pfahl, A., Buselmeier, M., and Zaschke, M. 2011. Wind loads on heliostats and photovoltaic trackers of various aspect ratios, *Solar Energy*, 85: 2185-201.

Pfahl, A., Buselmeier, M. Zaschke, M. 2011. Determination of wind loads on heliostats. In *Proceedings of the 17th SolarPACES Conference*. Spain.

Pfahl, A., Coventry, J., Röger, M., Wolfertstetter, F., Vásquez-Arango, J. F., Gross, F., Arjomandi, M., Schwarzbözl, P., Geiger, M., and Liedke, P. 2017. Progress in heliostat development, *Solar Energy*, 152: 3-37.

Pfahl, A., Randt, M., Meier, F., Zaschke, M., Geurts, C. P. W., and Buselmeier, M. 2015. A holistic approach for low cost heliostat fields, *Energy Procedia*, 69: 178-87.

Rasmussen, J. T., Hejlesen, M. M., Larsen, A., and Walther, J. H. 2010. Discrete vortex method simulations of the aerodynamic admittance in bridge aerodynamics, *Journal of Wind Engineering and Industrial Aerodynamics*, 98: 754-66.

Shu, Z. R., and Li, Q. S. 2017. An experimental investigation of surface pressures in separated and reattaching flows: Effects of freestream turbulence and leading edge geometry, *Journal of Wind Engineering and Industrial Aerodynamics*, 165: 58-66.

Simiu, E., and Scanlan, R. H. 1996. *Wind Effects on Structures*, John Wiley & Sons.

Sment, J., and Ho, C. K. 2014. Wind patterns over a heliostat field, *Energy Procedia*, 49: 229-38.

Téllez, F., Burisch, M., Villasente, Sánchez, M., Sansom, C., Kirby, P., Turner, P., Caliot, C., Ferriere, A., Bonanos, C. A., Papanicolas, C., Montenon, A., Monterreal, R., and Fernández, J. 2014. State of the Art in Heliostats and Definition of Specifications, *STAGE-STE Project, Madrid, Spain*.

von Kármán, T. 1948. Progress in the Statistical Theory of Turbulence, *Proceedings of the National Academy of Sciences*, 34: 530-39.

Watkins, S., Milbank, J., Loxton, B. J., and Melbourne, W. H. 2006. Atmospheric winds and their implications for microair vehicles, *AIAA Journal*, 44: 2591-600.

Wooding, R. A., Bradley, E. F., and Marshall, J. K. 1973. Drag due to regular arrays of roughness elements of varying geometry, *Boundary-Layer Meteorology*, 5: 285-308.